Development and Testing of a Multi-Plate Recuperative Heat Exchanger for Use in a Hybrid Cryocooler

D.W. Hoch[1], G.F. Nellis[1], N.L. Meagher[1], J.R. Maddocks[2], S. Stephens[3]

[1]University of Wisconsin-Madison
Madison, WI, 53706, U.S.A.
[2] Atlas Scientific
San Jose, CA, 95120, U.S.A.
[3]Air Force Research Laboratory
Kirtland AFB, NM, 87117, U.S.A.

ABSTRACT

Current available cryocooler technology operating at sub-10 K load temperatures is too massive and inefficient to be considered for future space-based systems. High vibrations and low reliability often cause these systems to limit the operating life relative to what is required of space flight hardware. A compact and innovative hybrid cryocooler is being developed that has the potential to provide a more efficient means of cooling future space-based systems [1]. The cooler directly interfaces a recuperative, reverse-Brayton, low-temperature stage with a regenerative, pulse-tube upper stage [2].

Four components of the PT/RB are critical to its performance: the pulse-tube cold head, the rectification system, the cryogenic turbine and the high effectiveness recuperative heat exchanger. The focus of this paper will be on the recuperative heat exchanger, which uses chemically etched copper plates interleaved with stainless steel axial conduction barriers. A model of the recuperative heat exchanger is described; the model is used to optimize the geometry subject to constraints associated with fabrication and mass. A sub-scale module has been fabricated in order to verify the model and develop the fabrication techniques. The experimentally measured ineffectiveness of the sub-scale module agrees with the model predictions. Based on the success of the sub-scale module and using the verified heat exchanger model, two full-scale modules have been fabricated, assembled and tested at the component level. The performance of the full-scale modules is compared with the model prediction.

INTRODUCTION

Futures space-borne missions will require cooling at or below 10 K. A compact and innovative hybrid cryocooler is being developed that will provide low vibration and long-lived cooling suitable for space flight. The hybrid cryocooler is based on the direct, fluid integration of a recuperative, reverse-Brayton, low-temperature stage with a regenerative, pulse-tube upper

Cryocoolers 14, edited by S.D. Miller and R.G. Ross, Jr.

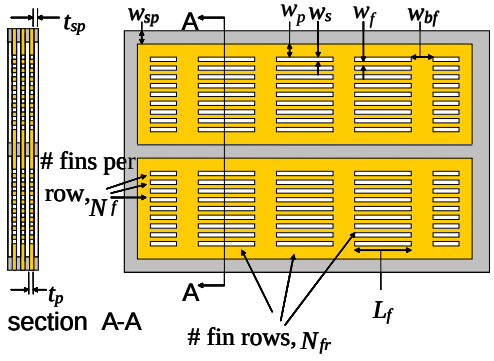

Figure 1. Geometric parameters of copper plate and stainless steel spacer.

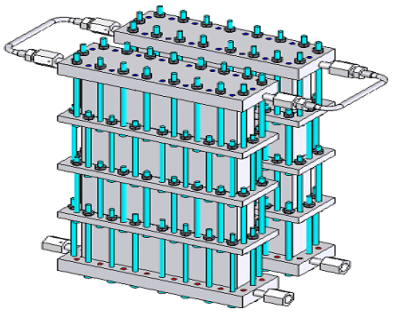

Figure 2. Solid model of recuperator showing modular, parallel-plate design.

stage. The continuous flow nature of the recuperative system allows relatively large loads to be accepted over a long distance with a small temperature difference. The hybrid system is substantially different from other hybrid cryocoolers, such as Gifford-McMahon/Joule-Thomson systems [3] or the Boreas refrigerator [4] and has some unique advantages relative to mechanical and electrical isolation.

This paper describes the development of the recuperative heat exchanger used in the pulse tube/reverse Brayton (PT/RB) hybrid cryocooler. The recuperative heat exchanger is a perforated plate type configuration in which chemically etched copper plates are interleaved with stainless steel axial conduction barriers. Figure 1 illustrates the Multi-Row Perforated Plate (MRPP) design and geometric parameters that must be defined to determine the thermal performance of the heat exchanger. The grey border in Figure 1 illustrates the stainless steel spacer.

The motivation behind having a multi-row geometry as opposed to the more typical geometry where all of the slots are perpendicular to the web of the spacer is that the chemical etching allows the use of very thin slots and fins which provide a large amount of surface area but cannot extend very far length-wise when placed perpendicular to the center web without becoming too resistive to conduction along the fin (i.e., the fin efficiency becomes too small). The result is either a very long, thin heat exchanger consisting of two very long rows of slots or complex headers with alternating high and low pressure regions. The MRPP concept avoids this by placing the slots parallel to the center web. This keeps the slot length reasonable but also provides relatively larger conduction paths between rows of slots.

The recuperative heat exchanger will be fabricated as 8 full-scale modules each consisting of 125 copper plates interleaved with an equal number of stainless steel spacers; this provides some risk reduction relative to brazing all of the required plates together into one stack. Two rows of 4 modules will be placed side by side and arranged in series in order to provide a reasonably sized heat exchanger that can fit within the shroud that is available in the vacuum vessel. This modular recuperator design allows each section to be individually leak checked; if a leak is detected it can be isolated and repaired. Irreparable damage to a single module will not put the entire heat exchanger at risk. Figure 2 illustrates a model of the full scale recuperator and headers.

A model of the recuperative heat exchanger is described in this paper and compared with experimental results.

MODEL DESCRIPTION

A computer model of the MRPP has been developed. The basic element of the model is a thermal model of a single plate. It is assumed that the fluid will completely mix in the space

between adjacent plates so that the temperature of the hot fluid is uniform as it enters all of the slots on the high-pressure side ($T_{h,in}$) and the temperature of the cold fluid is uniform as it enters all of the slots on the low-pressure side ($T_{c,in}$). The fluid passing through each fin row does not maintain a constant temperature; rather, its temperature will change due to its finite capacity rate. As a result of this, as well as axial (i.e., in the flow direction) temperature variations in the fin material, it is incorrect and non-conservative to use conventional fin equations that assume constant fluid temperature. A numerical model that solves the coupled differential equations governing the two-dimensional temperature distribution in the fluid and the fin material has been developed, validated, and nondimensionalized. The result of the numerical model is the prediction of the fin effectiveness (ε_f) as a function of the fin constant (β_f) and the fin number of transfer units (NTU_f), shown in Figure 3.

The fin effectiveness (ε_f) is defined as the ratio of the actual heat transfer through the base of the fin ($\dot{q}_f$) to the maximum possible heat transfer; i.e., the heat transfer that would occur if the fluid temperature was reduced or increased to the base temperature of the fin (T_b). On the high-pressure side this leads to:

$$\varepsilon_{f,h} = \frac{\dot{q}_f}{\left(\frac{\dot{m}}{N_f N_{fr}}\right) c_p \left(T_{h,in} - T_b\right)} \tag{1}$$

where c_p is the constant pressure specific heat capacity of the fluid. Note that because of the multi-row configuration, the base temperatures of the fins are not constant but instead vary depending on their location relative to the spacer. On the low-pressure side, the fin effectiveness is:

$$\varepsilon_{f,c} = \frac{\dot{q}_f}{\left(\frac{\dot{m}}{N_f N_{fr}}\right) c_p \left(T_b - T_{c,in}\right)} \tag{2}$$

The fin constant and fin number of transfer units are defined as:

$$\beta_f = \frac{L_f}{2}\sqrt{\frac{2h}{k_p w_f}} \tag{3}$$

$$NTU_f = \frac{2L_f t_p h N_f N_{fr}}{\dot{m} c_p} \tag{4}$$

where h is the heat transfer coefficient between the working fluid and the gas. Each of the curves for ε_f as a function of NTU_f in Figure 3 can be adequately represented by Eq. (5) which is a best fit to the numerical model results:

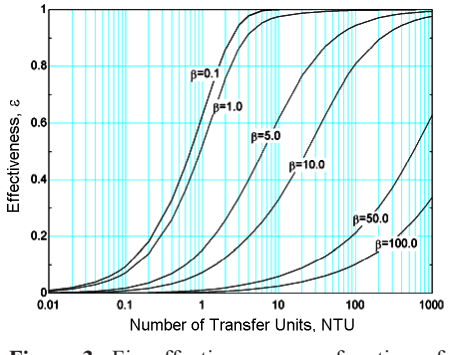

Figure 3. Fin effectiveness as a function of number of transfer units for several values of the fin constant.

Table 1. Constants required for analytical solution.

Index, i	a_i	b_i	c_i
0	0.297925119	0.927242296	-0.049798866
1	1.492222514	-0.071330646	-0.106555996
2	-0.081006078	0.061074063	0.020416859
3	0.002369923	0.026320276	0.141444269
4	-	-0.067908807	0.032192166
5	-	-0.03036481	-0.048599571
6	-	-	-0.018543303

$$\varepsilon_f = 1 - exp\left[-a\left(\beta_f\right) \cdot NTU_f^{\,b\left(\beta_f\right)+c\left(\beta_f\right)\cdot ln\left(NTU_f\right)} \right] \tag{5}$$

Equations for *a, b*, and *c* as functions of the fin constant are listed below and the required constants are contained in Table 1.

$$a\left(\beta_f\right) = exp\left[-a_0 \cdot \beta_f^{\left(a_1 + a_2 \cdot \beta_f + a_3 \cdot \beta_f^2\right)} \right] \tag{6}$$

$$b\left(\beta_f\right) = \sum_{i=0}^{5} b_i \cdot \left[log_{10}\left(\beta_f\right) \right]^i \tag{7}$$

$$c\left(\beta_f\right) = \sum_{i=0}^{6} c_i \cdot \left[log_{10}\left(\beta_f\right) \right]^i \tag{8}$$

Equations (3) through (8) allow the effectiveness of the fins to be predicted as a function of the fin constant and number of transfer units. The maximum error associated with the use of this analytical approximation in the range 0.01 < NTU < 1000 and 0.01 < β < 5 is 3.2% and the rms error over this range is 0.04%.

The hydraulic diameter of a slot (d_h) is:

$$d_h = \frac{2 L_f w_s}{L_f + w_s} \tag{9}$$

The mean velocity of the fluid within the slot (u_m) is:

$$u_m = \frac{\dot{m}}{L_f w_s N_f N_{fr} \rho} \tag{10}$$

where ρ is the fluid density. The Reynolds number for the flow (*Re*) through the slots on the high and low-pressure sides is given by:

$$Re = \frac{\rho d_h u_m}{\mu} \tag{11}$$

where μ is the fluid viscosity. For laminar flow (*Re*<2300), the Nusselt number (*Nu*) under fully developed conditions for a rectangular duct subject to a constant wall temperature is given by [5]:

$$Nu = 7.541\left(1 - 2.61\alpha + 4.97\alpha^2 - 5.119\alpha^3 + 2.702\alpha^4 + 0.548\alpha^5\right) \tag{12}$$

where α is the aspect ratio of the slot:

$$\alpha = \frac{\min\left(w_s, L_f\right)}{\max\left(w_s, L_f\right)} \tag{13}$$

Note that the use of Equation (12) is somewhat conservative in that the enhancement of heat transfer related to the developing region of the channel is neglected. The heat transfer coefficient in the slot is:

$$h = \frac{Nu\, k}{d_h} \tag{14}$$

Equations (1) and (2) may be written in the form of thermal resistances (R_f) that characterize the heat transfer rate as being driven by the difference between the fluid inlet temperature and the temperature at the base of the fins:

$$\dot{q}_f = \frac{\left(T_{h,in} - T_b\right)}{R_{f,h}} \quad \text{where } R_{f,h} = \frac{N_f N_{fr}}{\varepsilon_{f,h} \dot{m} c_p} \tag{15}$$

$$\dot{q}_f = \frac{\left(T_b - T_{c,in}\right)}{R_{f,c}} \quad \text{where } R_{f,c} = \frac{N_f N_{fr}}{\varepsilon_{f,c} \dot{m} c_p} \tag{16}$$

The resistance from the center-line of the material separating adjacent fin rows (T_{cl}) to the fluid inlet temperature (R_{cl}) is larger due to conduction through the plate material separating adjacent fin rows:

$$R_{cl,h} = R_{f,h} + \frac{w_{bf}}{2k_p\, t_p \left(w_s + w_f\right)} \tag{17}$$

$$R_{cl,c} = R_{f,c} + \frac{w_{bf}}{2k_p\, t_p \left(w_s + w_f\right)} \tag{18}$$

The material separating the fin rows acts essentially like another extended surface. Heat is transferred away from the spacer wall through this material via conduction; moving along the length of the material, heat is removed via conduction to the fins in the adjacent rows. It should be noted that there is a temperature drop both through the spacer material and through the fin material; this is the penalty associated with the multi-row vs. the more typical single-row configuration. An energy balance on a differential segment of the material between the fin rows on the high-pressure side leads to:

$$\frac{2\left(T_{cl} - T_{h,in}\right)}{R_{cl,h}\left(w_s + w_f\right)} = w_{bf}\, t_p\, k_p \frac{d^2 T_{cl}}{dz^2} \tag{19}$$

On the low-pressure side, the energy balance is:

$$\frac{2\left(T_{cl} - T_{c,in}\right)}{R_{cl,c}\left(w_s + w_f\right)} = w_{bf}\, t_p\, k_p \frac{d^2 T_{cl}}{dz^2} \tag{20}$$

where z is the direction perpendicular to the spacer material (i.e., the coordinate that runs along the material separating two rows of fins). The boundary conditions on these differential equations are a specified temperature at the fin row closest to the spacer wall and an adiabatic end condition.

$$T_{cl}\left(z = 0\right) = T_{cl,base} \tag{21}$$

$$\frac{dT_{cl}}{dz}\left(z = N_f\left(w_s + w_f\right)\right) = 0 \tag{22}$$

These equations are analogous to the fin equations and can be solved using a similar technique. The variable θ_h is defined according to:

$$\theta_h = T_{cl} - T_{h,in} \tag{23}$$

Substitution of θ_h into Equation (22) leads to:

$$\frac{d^2\theta_h}{dz^2} - m_h^2\, \theta_h = 0 \tag{24}$$

$$m_h^2 = \frac{2}{R_{cl,h}\left(w_s + w_f\right) w_{bf}\, t_p\, k_p} \tag{25}$$

The temperature distribution along the centerline of the material separating two fin rows is therefore:

$$T_{cl}\left(z\right) = T_{h,in} + \left(T_{cl,base} - T_{h,in}\right) \frac{\cosh\left[m_h\left(N_f\left(w_s + w_f\right) - z\right)\right]}{\cosh\left[m_h\, N_f\left(w_s + w_f\right)\right]} \tag{26}$$

The heat transfer rate into the base of the material separating two fin rows ($\dot{q}_{fr}$) is given by:

$$\dot{q}_{fr} = -k_p\, t_p\, w_{bf} \frac{dT_{cl}}{dz}\left(z = 0\right) \tag{27}$$

Substituting Equation (26) into Equation (27) leads to:

$$\dot{q}_{fr} = k_p\, t_p\, w_{bf}\, m_h \tanh\left[m_h\, N_f \left(w_s + w_f\right)\right]\left(T_{cl,base} - T_{h,in}\right) \tag{28}$$

Equation (28) can be rewritten in the form of a thermal resistance between the temperature of the inlet fluid and the plate material at $z = 0$.

$$\dot{q}_{fr} = \frac{\left(T_{cl,base} - T_{h,in}\right)}{R_{fr,h}} \text{ where } R_{fr,h} = \frac{1}{k_p\, t_p\, w_{bf}\, m_h \tanh\left[m_h\, N_f \left(w_s + w_f\right)\right]} \tag{29}$$

Considering all of the fin rows and the material associated with the plate material between the center of the spacer wall (at temperature T_{spacer}) and the first fin leads to the following equation for the total heat transferred in each plate ($\dot{q}_p$):

$$\dot{q}_p = \frac{\left(T_{spacer} - T_{h,in}\right)}{R_{plate,h}} \text{ where } R_{plate,h} = \frac{R_{fr,h}}{N_{fr}} + \frac{\left(w_p + \frac{w_{sp}}{2}\right)}{N_{fr}\, w_{bf}\, t_p\, k_p} \tag{30}$$

A similar equation can be written for the low-pressure side of the plate:

$$\dot{q}_p = \frac{\left(T_{spacer} - T_{c,in}\right)}{R_{plate,c}} \text{ where } R_{plate,c} = \frac{R_{fr,c}}{N_{fr}} + \frac{\left(w_p + \frac{w_{sp}}{2}\right)}{N_{fr}\, w_{bf}\, t_p\, k_p} \tag{31}$$

For the symmetric case considered here, the resistance associated with the two sides of the plate are identical ($R_{plate} = R_{plate,h} = R_{plate,c}$). The heat transferred in each plate is related to the average temperature change experienced by the fluid according to:

$$\dot{q}_p = \dot{m} c_P \left(T_{c,out} - T_{c,in}\right) \tag{32}$$

$$\dot{q}_p = \dot{m} c_P \left(T_{h,in} - T_{h,out}\right) \tag{33}$$

For the symmetric case considered here, the spacer temperature will be the average of the cold and hot inlet fluid temperatures:

$$T_{spacer} = \frac{T_{c,in} + T_{h,in}}{2} \tag{34}$$

Combining equations (30) through (34) leads to an expression for the effectiveness of an individual plate (ε_p):

$$\varepsilon_p \equiv \frac{\dot{q}_p}{\dot{m} c_P \left(T_{h,in} - T_{c,in}\right)} = \frac{1}{2\, R_{plate}\, \dot{m} c_P} \tag{35}$$

The resistance of a spacer to axial conduction (R_{spacer}) is:

$$R_{spacer} = \frac{t_{sp}}{k_{sp}\left(A_{HX}\, B_{HX} - \left(A_{HX} - 3\, w_{sp}\right)\left(B_{HX} - 2\, w_{sp}\right)\right)} \tag{36}$$

The total effectiveness of the heat exchanger is approximately:

$$\varepsilon = 1 - \left[1 + \frac{N_p\, \varepsilon_p}{1 - \varepsilon_p}\right]^{-1} - \frac{1}{\left(N_p + 1\right) R_{spacer}\, \dot{m} c_P} \tag{37}$$

where the 2nd term is a penalty associated with axial conduction.

Table 2. Summary of the specified geometry for the optimization of the full-scale MRPP.

Geometric Parameter	Symbol	SpecifiedValue
width of copper between slots	w_f	0.22 mm (0.0088 inch)
width of slots	w_s	0.18 mm (0.0072 inch)
thickness of plate	t_p	0.20 mm (0.008 inch)
thickness of spacer	t_{sp}	0.36 mm (0.014 inch)
width of spacer webs	w_{sp}	1.01 mm (0.040 inch)
width of plate material around spacer	w_p	1.01 mm (0.040 inch)
number of plates	N_p	1000

The pressure drop was calculated and found to be small under the operating conditions of the hybrid PT/RB cycle. Therefore, pressure drop does not strongly influence the performance of the recuperator.

OPTIMIZATION

During the optimization, several geometric parameters are specified; these are summarized in Table 2. A sub-scale module of this heat exchanger was built and tested; the thickness of the plate and spacer and the geometry of the slots and thickness between the slots specified in Table 2 are consistent with the sub-scale module. A total of 1000 copper plates are assumed which is consistent with a total heat exchanger length of nominally 56 cm (22 inch), excluding headers.

The unspecified values (i.e., the free parameters) include the length of the slots (L_f), the width of plate material between fin rows (w_{bf}), the number of fins in each row (N_f), and the number of fin rows on each side (N_{fr}). The optimization process constrains the heat exchanger mass to 10 kg while adjusting these free parameters in order to optimize the heat exchanger performance subject to the cycle operating conditions that provide between 0.5 W and 1.0 W of refrigeration load. The design of the optimized heat exchanger is summarized in Table 3.

EXPERIMENTAL FACILITY AND RESULTS

Leaks in the braze joints have been a problem during the manufacturing of the modules, but two modules were made leak tight after some post-brazing repair accomplished with indium solder. These two modules were bolted together in series using a stainless steel intermediate header piece. The intermediate header piece and the hot and cold headers were sealed using indium wire that was laid inside of an appropriately sized groove. The brazing process has been refined and additional modules are being manufactured at this time.

Component-level testing of the recuperative heat exchanger was accomplished in order to confirm the behavior of the device and verify the optimization process. This heat exchanger test is accomplished without the turbine and pulse tube components required for the hybrid PT/RB cycle. However, the inlet gas temperatures for the test must be near the nominal hybrid

Table 3. Summary of the optimization result.

Parameter	Symbol	Value
width of material between fin rows	w_{bf}	2.79 mm (0.110 inch)
length of slots	L_f	2.79 mm (0.110 inch)
number of fins per row	N_f	32
number of fin rows	N_{fr}	30
width of heat exchanger	B_{HX}	16.9 cm (6.65 inch)
thickness of heat exchanger	A_{HX}	3.31 cm (1.30 inch)
length of heat exchanger	H_{HX}	55.9 cm (22.01 inch)
mass of heat exchanger	M_{HX}	10.0 kg (22.0 lb_m)
effectiveness of heat exchanger	ε	0.9924

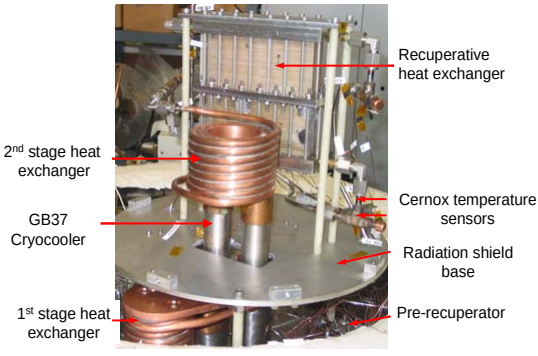

Figure 4. Key components of recuperator test facility.

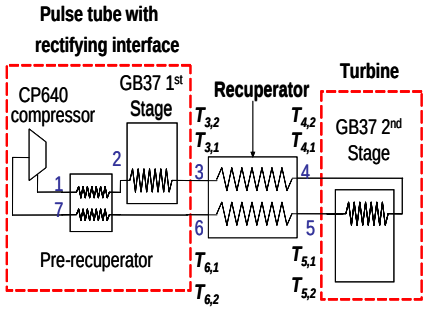

Figure 5. Schematic of the recuperator testing layout with boxes indicating the hybrid component being simulated.

operating temperatures; these test conditions were obtained using a Cryomech GB37, 2-stage cryocooler and suitable interface heat exchangers. An interface heat exchanger conductively coupled to the 1st stage of the GB37 combined with a pre-recuperator accomplishes the cooling that would otherwise be obtained from the pulse tube stage in a hybrid cycle. The 1st stage of the cryocooler was also used to conductively cool a copper radiation shield that limits the radiative parasitic to the recuperator modules under test. The cooling that would normally be provided by the turbine was replaced with an interface heat exchanger that is conductively coupled to the 2nd stage of the GB37, cooling the helium to sub-20 K temperatures. A Cryomech CP640 compressor was used to move the working fluid through the system. Figure 4 illustrates the two-module recuperator, first and second stage heat exchangers, cryocooler and radiation shield base. Figure 5 illustrates a schematic of the recuperator testing layout. During the recuperator test, the mass flow rate was held constant and the system was allowed adequate time to reach steady state before changing the flow rate. Figure 6 illustrates the measured hot and cold side effectiveness. The figure also shows the heat exchanger effectiveness predicted by the computer model which compares favorably with the experimental data.

Two Lakeshore Cernox sensors were used to measure the helium gas temperature at each inlet and outlet of the recuperator for a total of eight temperature measurements. One sensor at each inlet and exit was hermetically sealed inside of the plumbing to provide the most accurate gas temperature measurement. The second sensor for each inlet and exit was attached to the outside of the tubing using varnish; the external sensor was placed as close as possible to the penetration sensor in order to provide a redundant measurement.

The key measurement characterizing the ineffectiveness of the heat exchanger is the temperature difference between the in and out streams at the hot end and cold end of the recuperative heat exchanger. Therefore, before running the tests, the temperature sensors were calibrated in situ by mounting the cold in and hot out sensors in series and the hot out and cold in sensors in series. The response of the sensors was recorded as a function of the temperature of the fluid flowing across them and calibration curves were generated to ensure that the temperature difference between these sensors is measured quite accurately (more accurately than the absolute temperature of any one sensor).

Even with this careful calibration, there are several sources of temperature measurement uncertainty that must be accounted; these include data acquisition resolution, sensor self heating, excitation uncertainty, electromagnetic noise, calibration uncertainty, and mounting uncertainty. The magnitude of each of these sources of uncertainty was estimated; it was found that the most important sources of uncertainty are related to mounting (there is a consistent difference between the temperatures measured by the sensors located on the inside and outside of the tube in each location) and electromagnetic noise. The standard deviation in the temperature voltage signal of

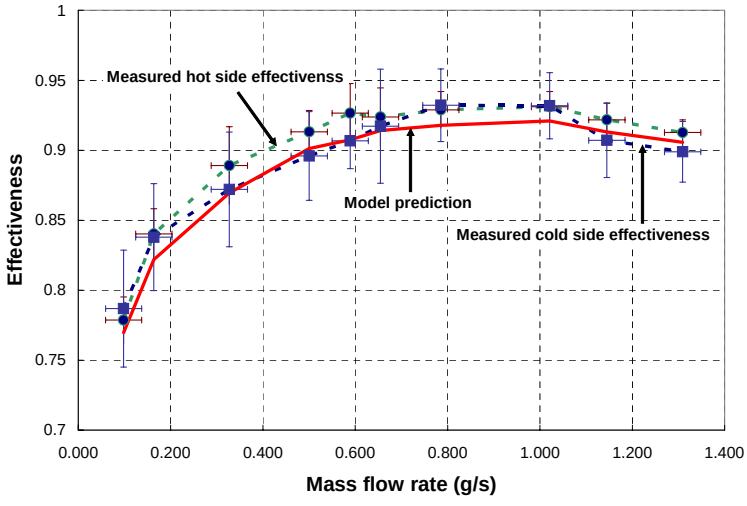

Figure 6. Heat exchanger effectiveness based on experimental data. The calculated effectiveness based on the computer model is also included.

each Cernox was calculated based on the last 30 data points for each steady state condition and used to quantify the uncertainty δT_{u1} due to electromagnetic noise:

$$\delta T_{u1} = \sqrt{\frac{n\sum x^2 - \left(\sum x\right)^2}{n(n-1)}} \tag{38}$$

where n is the number of data samples and x is the recorded voltage of each sample. Likewise, the last 30 data points were used to calculate an average temperature difference between the thermometers mounted on the inside and outside of the plumbing at each location:

$$\delta T_{u2} = T_{outside\_avg} - T_{inside\_avg} \tag{39}$$

The two errors were combined using the root-sum square (rss) formula to determine the total temperature uncertainty:

$$\delta T = \sqrt{\delta T_{u1}^2 + \delta T_{u2}^2} \tag{40}$$

The temperature uncertainty δT is likely somewhat conservative due to this method of estimating the mounting error; only the penetration measurements are used in the calculation and therefore the error associated with attaching the sensors externally vs. internally is not realized in the measurements. However, the difference between these sensor mounting configurations provides a reasonable methodology for estimating the general uncertainty associated with the mounting configuration.

The uncertainty in the effectiveness measured based on an energy balance on the hot side of the heat exchanger (δeff_{hot}) can be estimated according to:

$$\delta eff_{T_{h,in}} = \left(\frac{\partial eff}{\partial T_{T_{h,in}}}\right)\delta T \tag{41}$$

$$\delta eff_{T_{h,out}} = \left(\frac{\partial eff}{\partial T_{T_{h,out}}} \right) \delta T \tag{42}$$

$$\delta eff_{T_{c,in}} = \left(\frac{\partial eff}{\partial T_{T_{c,in}}} \right) \delta T \tag{43}$$

$$\delta eff_{hot} = \sqrt{\delta eff_{T_{h,in}}^2 + \delta eff_{T_{c,in}}^2 + \delta eff_{T_{h,out}}^2} \tag{44}$$

where $T_{h,in}$, $T_{h,out}$, and $T_{c,in}$ are the hot inlet, the hot outlet and the cold inlet temperatures, respectively. The uncertainty in the effectiveness measured based on an energy balance on the cold side of the heat exchanger is calculated using a similar procedure. The effectiveness based on the hot and cold side energy balance as well as their related uncertainty are displayed as *y*-axis error bars in Figure 6. The *x*-axis error bars in Figure 6 are related to the uncertainty in the OMEGA FMA1843 flow meter, which is ±3% of full scale or ± 0.3926 g/s of helium as stated by the manufacturer. The predicted effectiveness using the numerical model is also shown in Figure 6. Note that the two techniques for calculating effectiveness agree with each other to within the error bars which indicates that parasitic heat loss is adequately controlled and that the temperature measurement uncertainties have been estimated appropriately. Furthermore, the model prediction agrees with the measurements indicating that the 8 module recuperator should achieve the performance predicted in Table 3.

SUMMARY

A recuperative heat exchanger used in a pulse tube/reverse-Brayton hybrid cryocooler has been designed and tested. This design utilizes chemically etched copper plates that are interleaved with stainless steel axial conduction barriers. The measured heat exchanger effectiveness agrees with the model predictions.

ACKNOWLEDGMENT

Work supported by AFRL, Kirtland AFB under contracts F29453-03-C-02 and FA9453-04-C-0285 and FA9453-04-C-0285 and by NASA, Goddard Space Flight Center under contract NNG04CA69C.

REFERENCES

1. J. C. Evans, J. R. Maddocks, A. Kashani, D. W. Hoch, G. F. Nellis, B. Flake, T. Roberts, and T. Davis, 2006, "Progress towards a Pulse Tube/Reverse-Brayton Hybrid Cryocooler," *Advances in Cryogenic Engineering*, AIP, Melville, NY, Vol. 51, pp. 1481-1488.
2. A. K. Diab, G. F. Nellis, J. R. Maddocks, and S. Yarbrough, "Development of a Rectifying Interface for a Hybrid Pulse-Tube/Reverse-Brayton Cryocooler," 2003, *Advances in Cryogenic Engineering*, Vol. 49B, pp. 1777-1782.
3. Lia, L. X., Wang, L., Addessi, L., Miglionico, G., Martin, D., Leskowicz, J., McNeill, M., Yatauro, B., and Tallerico, T., 2002, "A Five-Watt, G-M/J-T Refrigerator for LHe Target at BNL", *Advances in Cryogenic Engineering*, Vol. 47, pp. 776-781.
4. Crunkleton, J. A., 1993, "A New Configuration for Small-Capacity Liquid-Helium-Temperature Cryocoolers", *Proceedings of the Seventh International Cryocooler Conference*, p. 187.
5. W. M. Rohsenow, J. P. Hartnett, and Y. I. Cho, *Handbook of Heat Transfer*, McGraw-Hill, New York, 1998.